

Effects of Quantum Delocalization on Structural Changes in Lennard-Jones Clusters<sup>†</sup>

Jason Deckman and Vladimir A. Mandelshtam\*

Chemistry Department, University of California at Irvine, Irvine, California 92697

Received: January 5, 2009; Revised Manuscript Received: March 22, 2009

The ground states of Lennard-Jones clusters ( $LJ_n$ ) for sizes up to  $n = 147$  are estimated as a function of the de Boer quantum delocalization length,  $\Lambda$ , using the variational Gaussian wavepacket method. Consequently, the  $n$ - $\Lambda$  phase diagram is constructed showing the ranges of stability of various structural motifs, including the Mackay and anti-Mackay icosahedra, several nonicosahedral but highly symmetric structures, and liquidlike (or disordered) structures. The increase in  $\Lambda$  favors more disordered and diffuse structures over more symmetric and compact ones, eventually making the liquidlike structures most energetically favorable.

## Introduction

Atomic clusters are frequently studied to investigate the fundamental nature of finite, many-body systems. They exhibit rich thermodynamic properties and display complex behavior that is sensitive to their size and the form of the interatomic potential. Additionally, with an increased interest in nanoscale materials and devices, they provide a simple means for understanding the physical characteristics, and particularly the quantum mechanical behavior, of these microscopic systems.

Rare gas atomic or molecular (e.g., hydrogen) clusters are often simulated using the Lennard-Jones (LJ) pair potential

$$V(r_{ij}) = 4\epsilon \left[ \left( \frac{\sigma}{r_{ij}} \right)^{12} - \left( \frac{\sigma}{r_{ij}} \right)^6 \right] \quad (1)$$

Despite the apparent simplicity of the LJ model and relative ease of its implementation, the LJ clusters display very complex behavior; obtaining accurate, well-converged results in simulations of the LJ clusters has always been a challenge for theoreticians. The design and optimization of better, more efficient algorithms is often ancillary to their study and comprises a large area of research in itself.

With some notable exceptions, for sizes  $n \leq 1000$  the global minima structures of  $LJ_n$  clusters are dominated by the icosahedral motif,<sup>1,2</sup> whereas the closed-packed structures start to be favorable only around  $n \approx 10^5$ .<sup>3</sup> The icosahedral global minima structures are typically characterized by the existence of a complete icosahedral core ( $n = 13, 55, 147, \dots$ ) surrounded by an overlayer, which can adopt two different packings: the anti-Mackay ( $n = 14$  to 30, 56 to 81, 85, ...) or Mackay ( $n = 31$  to 55, 82 to 147, ...). There are several exceptions corresponding to clusters ( $n = 74$  to 76, 98, 102 to 104, ...) that adopt nonicosahedral structures as their global minimum configuration. Some structures representative of these structural motifs are shown in Figure 1. The notations are similar to those of ref 4.

At finite temperatures, local energy minima start to contribute to the equilibrium properties of the cluster. The presence of different structural motifs that may be favorable for certain ranges of the parameters ( $n$  or  $T$ ) gives rise to size- or temperature-induced structural transitions resulting from competition between the energy and entropy. Even for relatively small sizes ( $n \approx 20$ ), the number of thermodynamically relevant

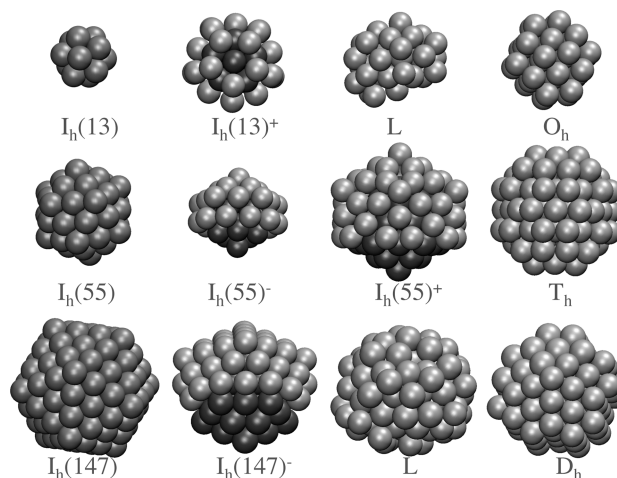


**Figure 1.** Selected images representative of the structural motifs encountered in the  $LJ_n$  clusters ( $n \leq 147$ ). The notations are similar to that of ref 4; namely,  $I_h(13)$ ,  $I_h(55)$ , and  $I_h(147)$  define the complete Mackay icosahedra with  $n = 13, 55$ , and 147.  $I_h(13)^+$  represents a structure ( $n > 13$ ) corresponding to a 13-atom complete Mackay icosahedron surrounded by an anti-Mackay overlayer.  $I_h(55)^-$  defines an incomplete icosahedron ( $n < 55$ ) based on  $I_h(55)$ . The octahedral (fcc), tetrahedral, and decahedral motifs are labeled, respectively,  $O_h$ ,  $T_h$ , and  $D_h$ . Liquidlike or disordered structures are labeled “L”.

minima for a LJ cluster is already very large and keeps increasing exponentially with size. Moreover, these minima are often separated by large barriers, leading to severe sampling problems. The replica exchange Monte Carlo method<sup>5</sup> is commonly employed to deal with such problems. The first successful application of the latter to an LJ cluster ( $n = 38$ ) was reported relatively recently,<sup>6</sup> which was then followed by a series of calculations covering a large range of sizes.<sup>7–11</sup> Reference 8 reports the size-temperature phase diagram of  $LJ_n$  clusters for ranges up to  $n = 147$ . Despite an apparent superiority of the replica exchange Monte Carlo to other methods, even with this technique, the computational times are usually very long. (For some extreme examples of poor convergence of the replica exchange method, see ref 11.)

Notwithstanding the difficulties of a classical simulation of LJ clusters, accurately modeling the quantum effects is further challenging. For smaller masses and at low temperatures, quantum effects become considerable, and if it is desired to

<sup>†</sup> Part of the “Robert Benny Gerber Festschrift”.

\* Corresponding author. E-mail: mandelsh@uci.edu.

elucidate the properties of real systems, accurately modeling them becomes necessary.

A quantum monatomic LJ system is conveniently parametrized by a single parameter, the de Boer quantum delocalization length  $\Lambda = (\hbar/(m\epsilon)^{1/2})/\sigma$ , which effectively measures the quantum delocalization of the ground-state wave function relative to the system scale defined by  $\sigma$ . For a given cluster size, the ground-state configuration depends on  $\Lambda$ , and with an increase (or decrease) in this value, structural changes occur, analogous to those induced by a change in temperature. For example, the study based on the path integral Monte Carlo (PIMC) method demonstrated that the melting of quantum LJ<sub>13</sub> cluster is facilitated by an increase in  $\Lambda$ .<sup>12</sup> In another paper,<sup>13</sup> the effects of quantum delocalization on the thermodynamic properties of several LJ<sub>*n*</sub> clusters were systematically studied using various approximate approaches. The more recent studies<sup>14,15</sup> demonstrated that whereas LJ<sub>38</sub> ( $\Lambda = 0$ ) possesses the octahedral ground-state configuration at  $T = 0$ , along with Ar<sub>38</sub> ( $\Lambda = 0.03$ ), the Ne<sub>38</sub> cluster ( $\Lambda = 0.095$ ) adopts the more disordered anti-Mackay configuration. Therefore, in addition to size-induced and temperature induced structural transitions, those induced by quantum effects can occur as well.

Quantum calculations using the PIMC methods, when converged, provide essentially exact results. However, when trying to describe structural transformations accurately using PIMC, the computation times can be excessively long and increase dramatically with decreasing temperature. The sampling problem already exists, such as for the characterization of a structural transition, where at least two basins of attraction (usually separated by a large energy barrier) must be sampled, regardless of whether the quantum effects are included in the simulation. In the PIMC framework, this corresponds to the sampling of the classical configuration space by the centroid of the path, whereas the sampling problem is alleviated by the presence of an additional much shorter time scale associated with the path variables describing the shape of the path. Strong quantum effects (such as quantum delocalization, tunneling, or both), as in helium systems, may effectively simplify the configuration space, removing the ergodicity problem and thus making the PIMC converge rapidly. However, it is the intermediate, that is, weakly quantum regime that is most challenging for accurate quantum simulations, especially for systems that undergo structural transformations at low temperatures. Examples of such systems include neon clusters, and, very likely, hydrogen clusters. Perhaps not surprisingly, the Ne<sub>13</sub> cluster is the largest neon system to undergo a low-temperature ( $T \approx 10$  K) structural change for which a converged heat capacity curve computed by the PIMC was reported.<sup>16</sup> Larger neon clusters, for example, Ne<sub>39</sub>, which undergo low-temperature structural changes<sup>17</sup> seem at the moment to be too difficult to be treated accurately by PIMC.<sup>18</sup>

Recently, several groups reported results on (H<sub>2</sub>)<sub>*n*</sub> clusters using diffusion Monte Carlo (DMC),<sup>19</sup> PIMC,<sup>20,21</sup> and path-integral ground state (PIGS)<sup>22</sup> methods. These calculations focused on studying the effects of either the superfluidity (i.e., taking into account the particle exchange symmetry) or the ground-state structure as a function of cluster size. All of the above-mentioned methods are, in principle, exact when converged. However, the results between any two references disagreed with each other on the detailed behavior of the chemical potential. (See below.) The lack of consensus in these results indicates that the sampling problems present a big challenge for the path-integral-based methods.

Faced with these difficulties, when studying the weakly quantum systems, it seems to be practical to use approximate methods that have better sampling properties but may still adequately account for the quantum effects. One such method utilizes the (Wigner–Kirkwood or Feynman–Hibbs) effective potentials.<sup>13</sup> Another approach is based on the harmonic approximation (HA).<sup>13</sup> To obtain the ground states using the HA for the entire range of  $\Lambda$ , one only needs to know the coordinates and the normal-mode frequencies of the local minima that are candidates for the ground-state at the corresponding values of  $\Lambda$ . For example, ref 3 presents an HA analysis of the ground-state structures of LJ clusters for specific values of  $\Lambda$  corresponding to different rare gas atomic clusters. Whereas the HA is straightforward to implement and it may be adequate for nearly classical cases, for example, xenon ( $\Lambda \approx 0.01$ ), krypton ( $\Lambda \approx 0.016$ ), or argon ( $\Lambda \approx 0.03$ ), in a more quantum regime, for example, corresponding to neon ( $\Lambda = 0.095$ ), the predictions of the HA are very crude.

Our method of choice for the estimation of cluster ground states is the variational Gaussian wavepacket (VGW) method.<sup>14,15,17,23</sup> The VGW is exact for a harmonic potential, whereas it is manifestly approximate for a general anharmonic potential. However, this method demonstrated its practicality, specifically for the case of Ne<sub>38</sub> (see ref 14), for which the VGW energies (more precisely, the energy differences of different cluster configurations) agreed very well with those computed by the PIMC method. We note here that the Gaussian form for the wave function is not invariant with respect to rotations of the cluster; that is, the rotational degrees of freedom are not represented correctly by the VGW, leading to a systematic error for the total energy of the cluster. Whereas for a sufficiently large cluster, this error is not significant, most importantly, it does not affect the energy differences between different cluster configurations because it is not sensitive to the latter.

In our previous work,<sup>15</sup> we used the VGW method to investigate the effect of changing the quantum parameter,  $\Lambda$ , on the ground-state configuration and energy for the range of clusters, LJ<sub>31–45</sub>, which, with the exception of LJ<sub>38</sub>, possess the Mackay classical global minimum. From this, structural changes as a function of  $\Lambda$  were investigated, and for the size range considered (except  $n = 38$ ), only two structural motifs were observed, I<sub>h</sub>(55)<sup>−</sup> and I<sub>h</sub>(13)<sup>+</sup>, that is, the Mackay and anti-Mackay icosahedra. Consequently, a “phase diagram” showing the stability ranges of the above structural motifs was constructed. In the present work, we extend our study up to the size  $n = 147$ , adding to the existing phase diagram.

The article continues with a brief but comprehensive description of the VGW approximation for determining the ground-state of a cluster, followed by a section comprising the computational results and discussion.

### Variational Gaussian Wavepacket Method for Estimating the Ground States of Clusters

In this section, we describe the method of estimating the ground-state energy and wave function of a many-body system using VGWs.

In Cartesian coordinates, the Hamiltonian is given by

$$\hat{H} = -\frac{\hbar^2}{2}\nabla^T\mathbf{M}^{-1}\nabla + U(\mathbf{r}) \quad (2)$$

with diagonal mass matrix  $\mathbf{M} = \text{diag}(m_i)$ . By  $\mathbf{r} := (\mathbf{r}_1, \dots, \mathbf{r}_n)^T$ , we define a  $3n$  vector containing the particle coordinates.  $\nabla := (\nabla_1, \dots, \nabla_n)^T$  represents the gradient.

The key assumption is that the ground-state wave function is well localized near one of the basins of attraction, typically one of the local potential energy minima. The trial wave function is then chosen in the form of a Gaussian

$$\Psi = \exp\left[-\frac{1}{2}(\mathbf{r} - \mathbf{q})^T \mathbf{G}^{-1}(\mathbf{r} - \mathbf{q}) + \gamma\right] \quad (3)$$

with the following variational parameters: the Gaussian width,  $\mathbf{G}$  (a  $3n \times 3n$  real symmetric and non-negative-definite matrix), the Gaussian center,  $\mathbf{q}$  (a real  $3n$  vector), and a real scale factor,  $\gamma$ . The ground-state energy is then estimated by minimizing the energy functional

$$E(\mathbf{q}, \mathbf{G}, \gamma) = \frac{\langle \Psi | \hat{H} | \Psi \rangle}{\langle \Psi | \Psi \rangle} \quad (4)$$

with respect to the above specified variational parameters.

Before proceeding further, the following points are important to emphasize.

(i) The VGW gives an exact solution for a Hamiltonian with harmonic potential; having the full-width matrix  $\mathbf{G}$  is essential unless one uses the normal mode coordinates, which cannot correspond to a general case.

(ii) It may appear that the VGW approximation is essentially equivalent to the harmonic approximation, in which each local minimum yields a quantum state, also being a Gaussian wave function. However, the latter Gaussian does not minimize the energy functional (eq 4) involving the actual Hamiltonian but rather its particular harmonic approximation. Moreover, the VGW approximation may still be adequate as long as the true ground-state wave function retains a bell-like shape, but it is possibly delocalized over more than one local minimum.<sup>14</sup> In the latter case, neither harmonic nor even anharmonic approximations would provide a qualitatively correct picture.

(iii) To obtain a systematic improvement of the solution, one may be tempted to generalize the single-Gaussian ansatz (eq 3) to a linear combination of Gaussians. Unfortunately, no matter how appealing the idea is, this possibility, at least for clusters, is illusory. First, without going into detail, numerically, the global optimization involving multiple Gaussians is an extremely difficult problem unless the Gaussian parameters are fixed. Second, if the basis contains more than one Gaussian, even if localized in a single local energy minimum, its size must be very large, otherwise the results could, in a certain sense, be worse than those from using a single Gaussian. For instance, note that because of the rotational invariance around the Euler angles for each local minimum, an adequate Gaussian basis must span at least the whole 3D rotational manifold. Third, having a Gaussian basis localized over more than one local minima is simply unfeasible. Finally, one has no way to assess the numerical errors associated with the multi-Gaussian approximation, for example, because these errors are partly due to the poor convergence of a particular global optimization attempt.

(iv) Minimization of  $E(\mathbf{q}, \mathbf{G}, \gamma)$  in eq 4 corresponds to the solution of a nonlinear global optimization problem, which is at least as difficult as minimization of the potential energy for the underlying classical system. As such, it should contain a local minimization step (called here quantum quenching) in which starting with some initial configuration  $\mathbf{q}_0$  the closest local minimum of  $E(\mathbf{q}, \mathbf{G}, \gamma)$  is found. Because, numerically, the energy functional (eq 4) possesses multiple local minima, to find the global minimum, one must perform a search over the whole configuration space. While the quenching step is system- and algorithm-specific, a search for the global minimum may use general global optimization strategies.

**TABLE 1: Parameters of the Gaussians (cf. Equation 5) Used to Approximate the LJ Potential,  $V(r_{ij}) = 4[(r_{ij})^{-12} - (r_{ij})^{-6}]$**

$p$	$c_p$	$\alpha_p$
1	31279960.65933084	35.14249661727566
2	1668963.963961670	21.73050942017830
3	91092.34069670191	13.25329843520143
4	3354.805129558428	7.60982070333635
5	-8.46844309983970	1.67180258175699
6	-0.38418467585210	0.50261814095335

To utilize eq 4 efficiently using the Gaussian ansatz (eq 3), the arising integrals are most conveniently evaluated by representing the pair potential as a sum of Gaussians

$$V(r_{ij}) \approx \sum_{p=1}^P c_p \exp(-\alpha_p r_{ij}^2) \quad (5)$$

with certain parameters  $c_p$  and  $\alpha_p$  ( $\text{Re } \alpha_p > 0$ ). For the LJ potential (eq 1), this approximation has proven to be practical with as few as three terms.<sup>23,24</sup> In the current work, for even more accurate approximation, a total of six Gaussians are used<sup>15,25</sup> with parameters given in Table 1.

The VGW is further characterized by two different forms, the fully coupled (FC) VGW, corresponding to the full  $3n \times 3n$  matrix  $\mathbf{G}$ , and the single particle (SP) VGW,<sup>23</sup> corresponding to a block-diagonal matrix  $\mathbf{G}$  composed of  $n$   $3 \times 3$  blocks. Whereas the SP-VGW does not provide an exact solution for a harmonic potential, numerically, it scales as  $\sim n^2$  with the system size  $n$ . (As for pairwise potentials, it requires an evaluation of an order of  $n^2$  terms.) The numerical scaling for the FC-VGW is  $\sim n^3$  (because of the need to evaluate the determinant of the full  $3n \times 3n$  matrix  $\mathbf{G}$ ), which may become computationally very demanding for sufficiently large systems.

The quantum quenching can possibly be performed by standard local minimization algorithms, as, for example, the steepest descent. However, because the VGW has already been implemented in the framework of quantum statistical mechanics calculations (see, e.g., refs 14 and 23), the quantum quenching here (as well as in refs 14 and 15) is carried out by solving the system of ordinary differential equations

$$\begin{cases} \frac{d}{d\tau} \mathbf{G} &= -\mathbf{G} \langle \nabla \nabla^T U \rangle_{\Psi} \mathbf{G} + \hbar^2 \mathbf{M}^{-1} \\ \frac{d}{d\tau} \mathbf{q} &= -\mathbf{G} \langle \nabla U \rangle_{\Psi} \\ \frac{d}{d\tau} \gamma &= -\frac{1}{4} \text{Tr}(\langle \nabla \nabla^T U \rangle_{\Psi} \mathbf{G}) - \langle U \rangle_{\Psi} \end{cases} \quad (6)$$

with initial conditions

$$\begin{aligned} \mathbf{q}(\tau_0) &= \mathbf{q}_0 \\ \mathbf{G}(\tau_0) &= \tau_0 \hbar^2 \mathbf{M}^{-1} \\ \gamma(\tau_0) &= -\tau_0 U(\mathbf{q}_0) \end{aligned} \quad (7)$$

which are defined for a sufficiently small but otherwise arbitrary value of  $\tau_0$ .

In eq 6,  $\langle U \rangle_{\Psi}$  represents the average (over the Gaussian wavepacket  $\Psi$ ) potential,  $\langle \nabla U \rangle_{\Psi}$  represents the averaged force, and  $\langle \nabla \nabla^T U \rangle_{\Psi}$  represents the averaged Hessian

$$\begin{aligned} \langle U \rangle_{\Psi} &:= \langle \psi | U | \psi \rangle \langle \psi | \psi \rangle^{-1} \\ \langle \nabla U \rangle_{\Psi} &:= \langle \psi | \nabla U | \psi \rangle \langle \psi | \psi \rangle^{-1} \\ \langle \nabla \nabla^T U \rangle_{\Psi} &:= \langle \psi | \nabla \nabla^T U | \psi \rangle \langle \psi | \psi \rangle^{-1} \end{aligned} \quad (8)$$

Given the Gaussian representation of the potential energy (eq 5), the following expressions can be used to evaluate the Gaussian integrals arising in eq 8.

Define the  $3 \times 3$  matrices

$$\mathbf{A}_{ij} := (\mathbf{G}_{ii} + \mathbf{G}_{jj} - \mathbf{G}_{ij} - \mathbf{G}_{ji})^{-1}$$

$$\mathbf{Z}_{ij}(\alpha) := \alpha - \alpha^2(\alpha + \mathbf{A}_{ij})^{-1}$$

where  $\mathbf{G}_{ij}$  denotes the corresponding  $3 \times 3$  block of the matrix  $\mathbf{G}$ . The analytic expression for the 3D Gaussian averaged over the variational Gaussian wavepacket then reads

$$\langle \exp(-\alpha r_{ij}^2) \rangle = \sqrt{\frac{\|\mathbf{A}_{ij}\|}{\|\mathbf{A}_{ij} + \alpha\|}} \exp[-\mathbf{q}_{ij}^T \mathbf{Z}_{ij}(\alpha) \mathbf{q}_{ij}] \quad (9)$$

where  $\mathbf{q}_{ij} := \mathbf{q}_i - \mathbf{q}_j$ . The elements of the averaged gradient are

$$\langle \nabla_k \exp(-\alpha r_{ij}^2) \rangle = -2 \langle \exp(-\alpha r_{ij}^2) \rangle \mathbf{Z}_{ij}(\alpha) \mathbf{q}_{ij} \quad (10)$$

for  $k = i, j$  and  $\langle \nabla_k \exp(-\alpha r_{ij}^2) \rangle = 0$ , for  $k \neq i, j$ . Finally, the four nonzero blocks of the second-derivative matrix are given by

$$\begin{aligned} \langle \nabla_i \nabla_i^T \exp(-\alpha r_{ij}^2) \rangle &= \langle \nabla_j \nabla_j^T \exp(-\alpha r_{ij}^2) \rangle \\ &= -\langle \nabla_i \nabla_j^T \exp(-\alpha r_{ij}^2) \rangle = -\langle \nabla_j \nabla_i^T \exp(-\alpha r_{ij}^2) \rangle \quad (11) \\ &= 2 \langle \exp(-\alpha r_{ij}^2) \rangle (2 \mathbf{Z}_{ij}(\alpha) \mathbf{q}_{ij} \mathbf{q}_{ij}^T \mathbf{Z}_{ij}^T(\alpha) - \mathbf{Z}_{ij}^T(\alpha)) \end{aligned}$$

The time-dependent wavepacket  $\Psi \equiv \Psi(\mathbf{q}, \mathbf{G}, \gamma)$  defined by the time-dependent parameters  $\mathbf{q} = \mathbf{q}_\tau$ ,  $\mathbf{G} = \mathbf{G}_\tau$ , and  $\gamma = \gamma_\tau$  is an approximation of the solution of the Bloch equation

$$\Psi(\mathbf{q}_0, \tau) = e^{-\tau \hat{H}} \Psi(\mathbf{q}_0, 0) \quad (12)$$

with  $\Psi(\mathbf{q}_0, 0) := \delta(\mathbf{r} - \mathbf{q}_0)$ .

Now define

$$E(\mathbf{q}_0, \tau) := \frac{\langle \Psi(\mathbf{q}_0, \tau/2) | \hat{H} | \Psi(\mathbf{q}_0, \tau/2) \rangle}{\langle \Psi(\mathbf{q}_0, \tau/2) | \Psi(\mathbf{q}_0, \tau/2) \rangle} \quad (13)$$

In the  $\tau \rightarrow \infty$  limit, independent of the initial configuration,  $\mathbf{q}_0$ , the exact solution of the Bloch equation,  $\Psi(\mathbf{q}_0, \infty)$ , will always coincide with the true ground-state wave function and so will the energy,  $E(\mathbf{q}_0, \infty)$ . However, with an approximate asymptotic solution, the stationary VGW will depend on  $\mathbf{q}_0$  and will usually become localized in the vicinity of  $\mathbf{q}_0$ . Therefore, even in the  $\tau \rightarrow \infty$  limit,  $E(\mathbf{q}_0, \tau)$  can only represent an upper-bound estimate for the true ground-state energy, whereas for obtaining an adequate estimate of the ground-state energy and wave function, one needs to sample a large number of stationary Gaussian states.

The energy  $E(\mathbf{q}_0, \tau)$  can be calculated by direct evaluation of eq 13. However, it is easier to use

$$E(\mathbf{q}_0, \tau) = \frac{d}{d\tau} \ln \rho(\mathbf{q}_0, \tau) \quad (14)$$

where we have defined the time-dependent density

$$\rho(\mathbf{q}_0, \tau) := \langle \Psi(\mathbf{q}_0, \tau/2) | \Psi(\mathbf{q}_0, \tau/2) \rangle \quad (15)$$

Assuming the Gaussian form for  $\Psi$  we have

$$\rho(\mathbf{q}_0; \tau) = (4\pi)^{-3n/2} \|\mathbf{G}(\tau/2)\|^{-1/2} \exp[2\gamma(\tau/2)]$$

As in ref 15, the initial configurations ( $\mathbf{q}_0$ ) to be quenched are generated by performing long replica exchange Monte Carlo simulations for a reference classical system. The configurations are taken from the random walks running at different temperatures once in many Monte Carlo steps (e.g.,  $10^5$  because it is numerically very cheap). The highest replica temperature in the classical simulation is chosen to be high enough to ensure the ergodicity of all of the random walks. To warrant an ade-

quate sampling of the whole configuration space, that is, to include all relevant structural motifs in the quantum quenching procedure, the initial configurations for quenching are selected from a sufficiently wide temperature range.

Here the reference classical system is defined by the actual potential energy  $U(\mathbf{r})$ , although a more efficient sampling could be achieved by using an effective potential.

## Results and Discussion

In ref 15, only  $\text{LJ}_n$  clusters with sizes  $n = 31$  to 45 were considered.  $\text{LJ}_{31}$  is the smallest cluster with global minimum belonging to the  $\text{I}_h(55)^-$  motif.  $\text{LJ}_{45}$  is the largest cluster that can have a structure defined by  $\text{I}_h(13)^+$  with a single anti-Mackay overlayer. The present article extends the ground-state calculations up to  $n = 147$ , the largest size of a three-layer cluster with icosahedral symmetry. For the two-layer clusters, here we included all remaining sizes ( $n = 46$  to 55). As  $n$  increases, the VGW calculations become increasingly more time-consuming. To reduce the computational burden, we considered only (approximately) every fifth three-layer cluster.  $\text{LJ}_{82}$  is the smallest cluster with global minimum belonging to the  $\text{I}_h(147)^-$  motif, so in addition, to better describe the onset of the  $\text{I}_h(147)^- \rightarrow \text{I}_h(55)^+$  transition, we analyzed the ground states for sizes  $n = 82$  to 89, at least in the range of the low  $\Lambda$  values. We also analyzed the low- $\Lambda$  range for all of the cases of nonicosahedral global energy minima ( $n = 75$  to 77, 98, 102 to 104).

The classical replica exchange method<sup>5</sup> was used to sample the configuration space. The details of the classical simulation, which are not of crucial importance for this particular application, can be found in ref 8. Depending on the cluster size, the total number of replicas varied between 10 and 15, with the maximum temperature  $T_{\text{max}} = 0.4$ . Here and throughout the article the reduced units for the temperature,  $\epsilon k_B^{-1}$ , and energy ( $\epsilon$ ) are used. To convert to the actual temperature or energy for a particular species, one needs to know the corresponding LJ parameter,  $\epsilon$ . For example, for neon,  $\epsilon(\text{Ne}) = 35.6 k_B$  K.

The configurations for quenching were selected from several (typically eight) random walks, once in every  $10^5$  MC steps, running at temperatures around Mackay/anti-Mackay and anti-Mackay/liquid transitions in the corresponding classical system.<sup>8</sup> For each cluster, this resulted in a total of about  $8 \times 10^4$  configurations. For each configuration, the quantum quenching was first performed using the SP-VGW with  $\Lambda = 0.19$  and 0.30 up to  $\tau = 5$  (or  $T = 0.2$ ).

At the end of the replica exchange simulation, for each of the  $\Lambda$  values used, the 100 lowest energy configurations were retained. The latter were then quenched again but now using the FC-VGW. In addition, we made sure that for each  $n$ , the global classical potential energy minimum<sup>26</sup> was also included. Each of the above quenched configurations was then propagated in  $\Lambda$  using a fine grid in the range  $\Lambda \in [0.00001, 0.32]$ .

To capture more liquidlike configurations for larger sizes ( $n \geq 90$ ), quenching was also performed at  $\Lambda = 0.33$ . However, we note that at this and higher values of  $\Lambda$ , the clusters become very unstable with respect to evaporation. (This problem could be dealt with by using a constraining potential rather than a constraining box, as implemented in the present study.) Therefore, to produce the energy curves  $E_i(\Lambda)$  for even higher values of  $\Lambda$ , we used curve extrapolation rather than quenching.

For each cluster size  $n$  we constructed a correlation diagram displaying the energy curves,  $E_i(\Lambda)$ , generated by the procedure described above. Two examples of such diagrams are shown in Figure 2. The energy curves are generally continuous in  $\Lambda$ , whereas the discontinuities sometimes occur for liquidlike

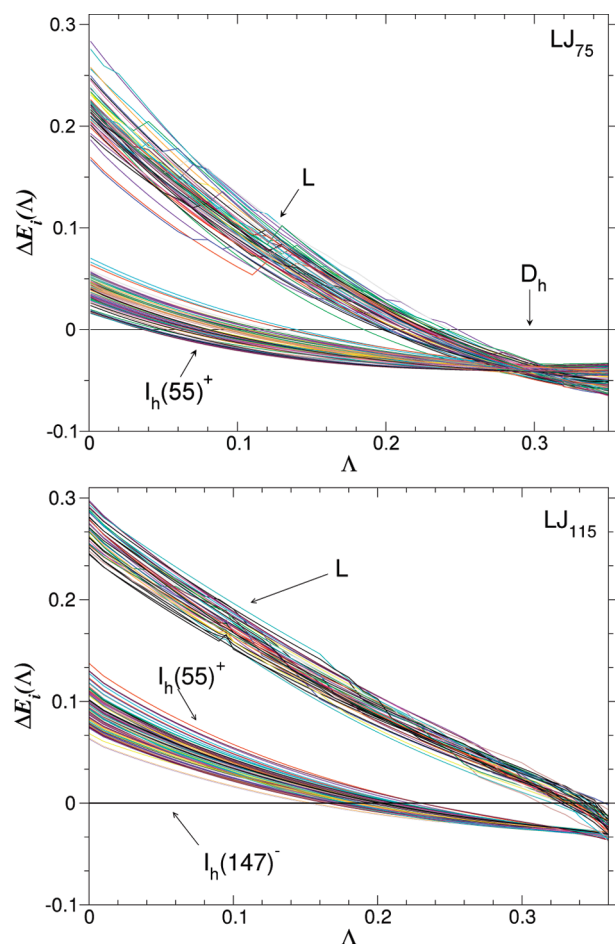


**Figure 2.** Correlation diagrams for LJ<sub>75</sub> and LJ<sub>115</sub> showing the relative energies per atom (in units of  $\epsilon$ ) of various configurations,  $\Delta E_i(\Lambda) := [E_i(\Lambda) - E_0(\Lambda)]/n$ , as a function of  $\Lambda$ , where  $E_i(\Lambda)$  is the cluster energy for  $i$ th configuration, with  $i = 0$  corresponding to the global classical energy minimum. Each band represents a particular structural motif, as indicated in the Figure.

configurations, indicating that at certain  $\Lambda$  values these configurations become unstable. Such an instability is expected because liquidlike local minima are not deep, and the energy barriers separating them are not high. For each  $\Lambda$ , the configuration having the lowest energy provides an estimate for the ground-state energy and structure. The structural identification was done either by using the orientational bond-order parameters  $Q_6$  and  $Q_4^{27}$  or by visual inspection. We note that no matter how many configurations have been sampled, the actual number of local minima is always orders of magnitude larger; that is, there is always a possibility that the lowest energy configuration has not been found. This is especially true for the liquidlike configurations. However, as can be seen from the diagrams, the energies of the sampled configurations tend to form bundles, each bundle corresponding to a particular structural motif. The energy curves within a single bundle are very close (often crossing each other and thus changing their relative stability). The latter circumstance makes us believe that even with the limited sampling of the configuration space, our conclusions about the ground-state energy and structure as a function of  $\Lambda$  are correct, at least qualitatively, assuming that the Gaussian approximation is adequate.

The analysis of the correlation diagrams for the cluster sizes considered resulted in the identification of the stability ranges of the structural motifs depicted in Figure 1. Each of the nonicosahedral structures ( $O_h$ ,  $T_h$ ,  $D_h$ ) becomes unstable at a

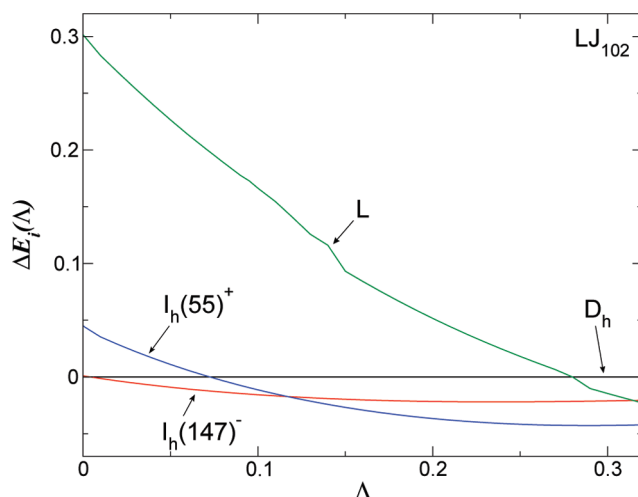


**Figure 3.** Same as Figure 2 but for LJ<sub>102</sub> and depicting only the lowest energy curve for each structural motif. The structural transitions occur where the curves intersect each other.

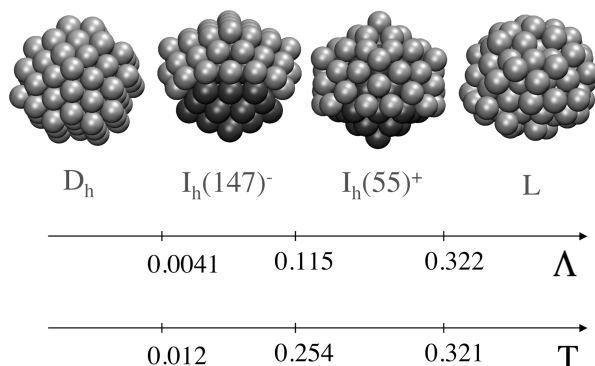


**Figure 4.** Four configurations of LJ<sub>102</sub> cluster involved in Figure 3. The darker color is used to identify the core atoms in the Mackay and anti-Mackay structures. The  $\Lambda$  and  $T$  axes identify the values of the corresponding structural transitions for respectively quantum ( $T = 0$ ) and classical ( $\Lambda = 0$ ) cases.

certain (sometimes very small) value of  $\Lambda$ . One such example is the LJ<sub>102</sub> cluster, which, in addition to the two generic transitions,  $I_h(147)^- \rightarrow I_h(55)^+$  and  $I_h(55)^+ \rightarrow L$ , undergoes the  $D_h \rightarrow I_h(147)^-$  transition at  $\Lambda \approx 4.1 \times 10^{-3}$ . The corresponding correlation diagram, which shows only one energy curve per structural motif, is given in Figure 3. The four ground-state structures involved in this Figure are shown in Figure 4.

All of the identified  $\Lambda$  values corresponding to the structural transformations in LJ<sub>*n*</sub> clusters are summarized in Table 2. The resulting “phase diagram” that shows the stability regions for different structural motifs as a function of  $n$  and  $\Lambda$  is given in Figure 5. This Figure also shows the size–temperature ( $n$ – $T$ ) phase diagram of the classical ( $\Lambda = 0$ ) LJ<sub>*n*</sub> clusters.<sup>8,11</sup> There is a striking resemblance of the two diagrams because in each of them, one can find the same structures stable over certain ranges of parameters. However, one must be careful in characterization or interpretation of the “disordered” or “liquidlike” structures. In particular, “liquidlike” does not mean “liquid”. The former is characteristic of the structure that is disordered, whereas the latter usually refers to certain kinetic properties of the state. Note that just like a glass state of a bulk system, a disordered state of a cluster in its ground state is actually completely frozen, although from the structural point of view, these states cannot be distinguished from those obtained by quenching truly liquid configurations of the cluster.

**TABLE 2: Values of  $\Lambda$  at Which the Quantum-Mechanically-Induced Structural Transformations Occur in  $LJ_n$  Clusters<sup>a</sup>**

$n$	$\Lambda_{s \rightarrow s}$	$\Lambda_{M \rightarrow aM(L)}$	$n$	$\Lambda_{s \rightarrow s}$	$\Lambda_{M \rightarrow aM(L)}$	$\Lambda_{M \rightarrow L}$
31		0.0167	60			0.2508
32		0.0248	65			0.2169
33		0.0345	70			0.2675
34		0.0240	75	0.0368		0.2760
35		0.0458	76	0.0166		*
36		0.0772	77	0.0179		*
37		0.0657	80			0.2945
38	0.0821	0.0895	82		0.0262	0.3081
39		0.1211	83		0.0525	*
40		0.1121	84		0.0344	*
41		0.1071	85			0.3269
42		0.1149	86		0.0094	*
43		0.1269	87		0.0282	*
44		0.1266	88		0.0488	*
45		0.1538	89		0.0997	*
46		0.1712	90		0.1153	0.3213
47		0.1970	95		0.0807	0.3442
48		0.2128	98	0.0008	0.1361	0.3406
49		0.2282	100		0.1441	0.3340
50		0.2446	102	0.0041	0.1169	0.3222
51		0.2689	103	0.0050	*	*
52		0.2930	104	0.0025	*	*
53		0.2918	105		0.1078	0.3403
54		0.2810	110		0.1519	0.3477
55		0.2737	115		0.1116	0.3540
			120		0.1090	0.3536
			125		0.1569	0.3501
			130		0.2035	0.3678
			135		0.2333	0.3857
			140		0.2841	0.3962
			145		0.3062	0.3890
			147		0.3102	0.4121

<sup>a</sup> Labels “M” and “aM” define, respectively, the Mackay and anti-Mackay structural motifs; “s  $\rightarrow$  s” stands for solid–solid transition. \* means that the corresponding value has not been computed. The anti-Mackay and liquidlike motifs for the two-layer clusters ( $n \leq 55$ ) could not be well distinguished.

Quantum delocalization always stabilizes the anti-Mackay relative to the Mackay structure with the well-identified quantum-mechanically induced Mackay/anti-Mackay transition. Further increase in  $\Lambda$  eventually destabilizes the anti-Mackay structure, resulting in the least-ordered liquidlike structure. However, for small two-layer clusters, we were not able to clearly distinguish between liquidlike and anti-Mackay structures. The probable reason is that the 13-atom icosahedral “core” is typically not unique for an anti-Mackay structure (i.e., there may be several 13-atom subclusters having the same arrangement of the complete icosahedron), whereas the 12-atom coordination is also characteristic of liquidlike structures. Interestingly, a similar difficulty was encountered when analyzing the temperature-induced structural changes in classical  $LJ_n$  clusters,<sup>8</sup> for which the liquidlike and anti-Mackay structural motifs could clearly be distinguished only for three-layer clusters ( $55 < n \leq 147$ ), the existence of the well-ordered complete-icosahedral 55-atom core being a unique property of the icosahedral motif. For the latter clusters, the heat capacity curve also displays a sharp peak at the temperature of the  $I_h(55)^+ \rightarrow L$  transition (also identified as the “core melting transition”). For the classical two-layer LJ clusters ( $n < 55$ ), only the  $I_h(55)^- \rightarrow I_h(13)^+$  transition can be identified unambiguously and is always accompanied by a sharp heat capacity peak. Furthermore, this peak gradually changes as a function of cluster size and continues into the size region ( $n > 45$ ), where the structures

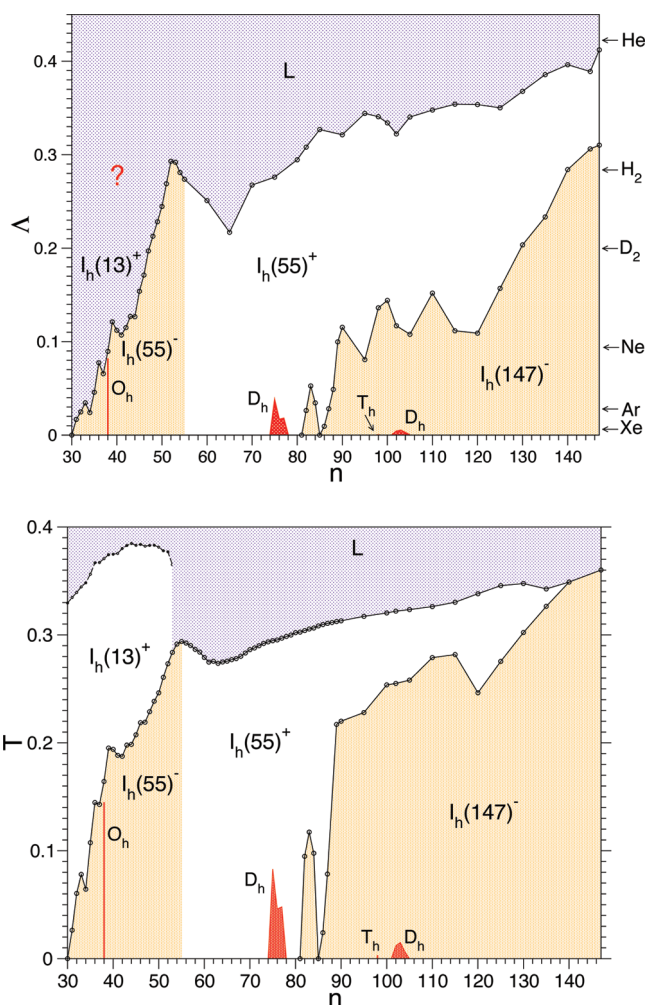


**Figure 5.**  $n$ – $\Lambda$  phase diagram (top) showing the stability ranges for the ground-state structures of quantum  $LJ_n$  clusters ( $n = 31$  to 147). The points are taken from Table 2. They are connected for better visualization. The question mark indicates the difficulty in distinguishing between anti-Mackay and liquidlike structures for two-layer clusters. Bottom: the corresponding  $n$ – $T$  phase diagram, which bears similarity to the top figure. This diagram was constructed using the data from refs 8 and 11.

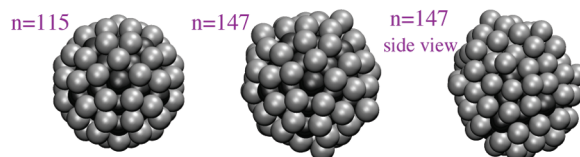


**Figure 6.** Images of anti-Mackay,  $I_h(55)^+$ , structures of  $LJ_{115}$  and  $LJ_{147}$ , each characterizing the ground state of the corresponding cluster stable over a certain  $\Lambda$  range.  $n = 115$  is the largest cluster belonging to the  $I_h(55)^+$  motif with a single anti-Mackay overlayer. For  $n > 115$ , the extra atoms fill the next layer, forming a double anti-Mackay overlayer, which can be seen in the side view.

identified by  $I_h(13)^+$  with a single anti-Mackay overlayer do not exist. That is, if one follows the  $I_h(55)^- \rightarrow I_h(13)^+$  transition as a function of cluster size, starting with small sizes ( $n \geq 31$ ), it gradually changes in character and for  $n > 55$  merges with the  $I_h(55)^+ \rightarrow L$  transition.

Figure 6 shows two examples of anti-Mackay,  $I_h(55)^+$ , ground-state structures for  $n = 115$  (the stability range is  $\Lambda \in [0.1116, 0.3540]$ ) and  $n = 147$  ( $\Lambda \in [0.3102, 0.4121]$ ). Although the largest structure with a single-anti-Mackay overlayer surrounding the 55-atom Mackay icosahedral core corresponds to

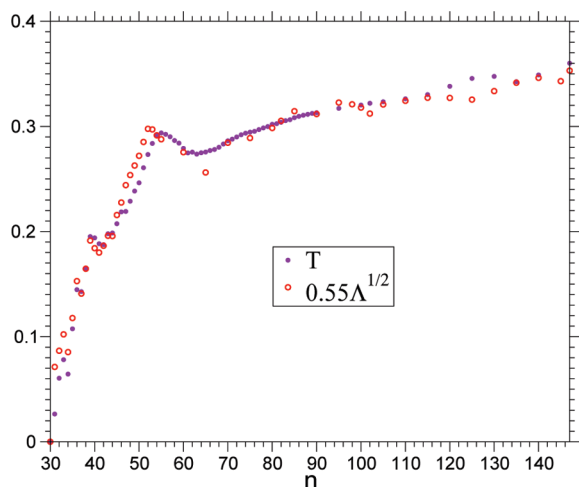


**Figure 7.** Attempt to find an effective temperature,  $T$ , for the classical  $LJ_n$  clusters that represents the corresponding quantum system with finite value of the quantum parameter  $\Lambda$ . The graph suggests that  $T \approx 0.55\Lambda^{1/2}$ . The filled and open circles give, respectively, temperatures and  $\Lambda$  values of the  $I_h(55)^+ \rightarrow L$  transition for  $n > 55$ . For  $n < 55$ , the transition corresponds to  $I_h(55)^- \rightarrow L$ ; further decrease of  $n$  gradually changes its character to the  $I_h(55)^- \rightarrow I_h(13)^+$  transition. Other types of classical/quantum transitions (not shown) do not match.

$LJ_{115}$  (having a perfect, nearly spherical shape), for  $n > 115$ , structures with double-anti-Mackay overlayer can become energetically favorable and are easily identified, as in the case of  $LJ_{147}$ . Note also ref 9, where two temperature-induced structural transformations were observed for the classical  $LJ_{309}$  cluster, whose global minimum is a complete four-layer Mackay icosahedron. In the latter work, the lower-temperature transition was interpreted as “surface roughening” of the overlayer surrounding the 147-atom Mackay icosahedral core.

For the lack of both a rigorous and simple method, one is often tempted to incorporate the quantum effects into the molecular dynamics simulations by using an “effective temperature”. The comparison of the classical  $n-T$  ( $\Lambda = 0$ ) and quantum  $n-\Lambda$  ( $T = 0$ ) diagrams (cf. Figure 5) suggests that such a mapping can be done on a certain level. In particular, we found empirically that the effective temperature defined by the relationship

$$T \approx 0.55\Lambda^{1/2} \quad (16)$$

results in good agreement between the classical,  $T(n)$ , and quantum,  $\Lambda(n)$ , melting curves. To demonstrate this in Figure 7, we plot the  $T$  and  $\Lambda$  values (scaled according to eq 16) of the  $I_h(55)^+ \rightarrow L$  ( $n > 55$ ) and  $I_h(55)^- \rightarrow I_h(13)^+/L$  ( $n < 55$ ) transitions. Unfortunately, the mapping (eq 16) is not universal because it gives disagreement for some other types of transitions, which display much greater size-sensitivity. Moreover, in the  $n-T$  ( $\Lambda = 0$ ) diagram, the  $I_h(147)^- \rightarrow I_h(55)^+$  and  $I_h(55)^+ \rightarrow L$  transition temperatures merge for  $n \geq 140$ , whereas in the  $n-\Lambda$  ( $T = 0$ ) diagram, these transitions for the same size range occur at different values of the quantum parameter.

Another interesting parallel exists between the present  $n-\Lambda$  diagram for the quantum  $LJ_n$  clusters and  $n-\rho$  diagram for the global minima structures of the classical Morse clusters,<sup>28,29</sup> where  $\rho$  is the range of the Morse potential defined by

$$U_{\text{Morse}}(r) = \epsilon e^{\rho(1-r/\sigma)} (e^{\rho(1-r/\sigma)} - 2) \quad (17)$$

The larger the  $\rho$  value, the shorter the range of the potential. For example, approximating the LJ potential by the Morse potential gives  $\rho \approx 6$ . Increasing the range of the potential

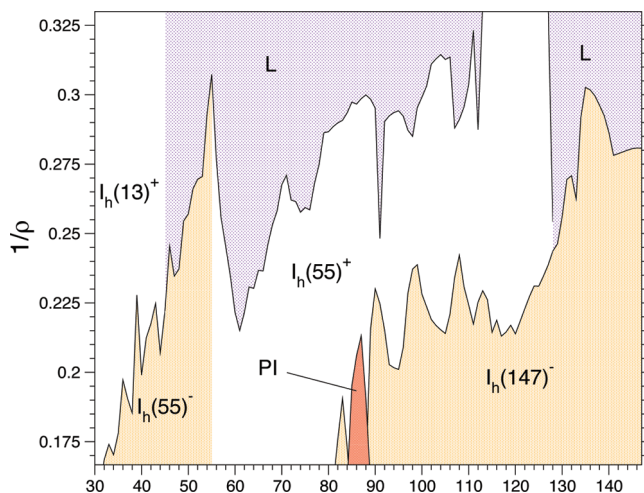


**Figure 8.** Phase diagram constructed with data from ref 4 for Morse clusters for the size range considered herein. “PI” labels the polyicosahedral motif, characterized by two complete icosahedral cores stuck together. Note that the LJ potential approximately corresponds to the Morse potential with  $\rho \approx 6$  ( $1/\rho \approx 1.667$ ).

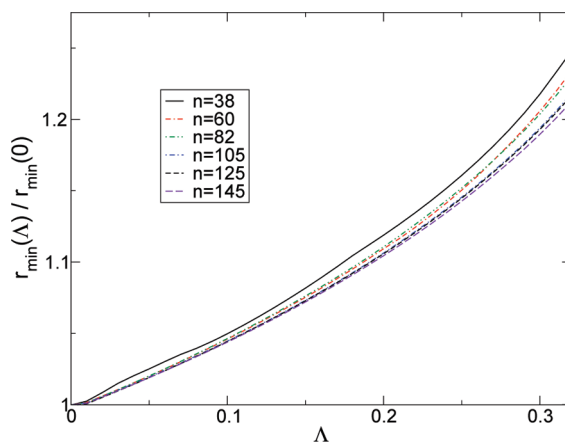


**Figure 9.** Effect of increasing  $\Lambda$  on interatomic distance for several different clusters, where  $r_{\min}$  defines the smallest interatomic distance for a given cluster.

destabilizes the Mackay (relative to the anti-Mackay) structures. Further increase in the range eventually makes the liquidlike structures energetically most favorable. A recent paper<sup>4</sup> reports a much more comprehensive  $n-\rho$  “phase diagram” for Morse clusters. A relevant part of this diagram is shown in Figure 8. In view of this comparison, we conclude that the quantum delocalization, besides making the effective pair interaction softer, also increases its range. The quantum order–disorder transition in the present case has nothing to do with quantum tunneling, nor does it involve any superfluidity because the exchange symmetries are not taken into account within the VGW approximation.

The increase in the range of the effective potential caused by the increase in quantum delocalization results in turn in the increase in the equilibrium interatomic distances in the cluster. This effect is demonstrated in Figure 9, where the minimum interatomic distance for different clusters is shown as a function of  $\Lambda$ .

Whereas the  $n$  and  $\Lambda$  dependences of the ground-state energies are featureless (and, therefore, not shown here), one can gain some insight from looking at the energy differences, or so-called “chemical potential”

$$\mu(n) = E(n) - E(n-1) \quad (18)$$

Local minima of  $\mu(n)$  correspond to more stable clusters relative

to their neighbors. The  $\mu(n)$  dependencies for values of  $\Lambda$  corresponding to Xe, Ne, D<sub>2</sub>, and H<sub>2</sub> are shown in Figure 10. As expected, the increase in  $\Lambda$  leads to the reduction of  $\mu(n)$ . Interestingly, strong correlations between the  $\mu(n)$  at different values of  $\Lambda$  with respect to size ranges having the same structural motif (i.e., Mackay) are clearly seen. For example, upon visual inspection, the curves for  $\Lambda(\text{Xe})$  and  $\Lambda(\text{Ne})$  for the size range corresponding to the I<sub>h</sub>(55)<sup>-</sup> motif ( $n = 39$  to  $54$ ), the oscillations appear to be nearly identical, although the curves pertain to significantly different quantum parameter. Conversely, no correlation can be seen for the range on these two curves ( $n = 31$  to  $38$ ) that share different ground-state motifs. For the  $\Lambda(\text{D}_2)$  and  $\Lambda(\text{H}_2)$  curves, in the range where both share the I<sub>h</sub>(13)<sup>+</sup> motif,  $n = 31$  to  $55$ , the lines show the same general trends; that is, maxima and minima correlate for both at respective  $n$ . This is in contradiction with the results reported in ref 22 for (H<sub>2</sub>)<sub>n</sub> and (D<sub>2</sub>)<sub>n</sub> clusters using the PIGS method, where no correlations exist between the H<sub>2</sub> and D<sub>2</sub> cases. These qualitatively different behaviors can hardly be accounted for by the different interaction potential used in the cited work.

## Conclusions

In this article, we extended our previous studies of the quantum-induced structural transitions in LJ<sub>n</sub> clusters to sizes up to  $n = 147$ . A convenient measure of quantum effects is the de Boer quantum delocalization length,  $\Lambda$ , which relates the particle mass,  $\hbar$ , and the two LJ parameters to the extent of delocalization of the ground-state wave function. Consequently, we constructed a  $n$ - $\Lambda$  ( $T = 0$ ) phase diagram that shows the ranges of stability of various structural motifs, such as Mackay icosahedral, anti-Mackay icosahedral, and liquidlike (or disordered) motifs. In addition, nonicosahedral structures are included for several cluster sizes. A particularly new finding of the present work is that the quantum delocalization eventually stabilizes the liquidlike structures, besides favoring the icosahedral structures over the nonicosahedral ones or, within the icosahedral

motif, favoring the anti-Mackay over Mackay structures. Whereas we were able to distinguish the anti-Mackay and liquidlike structural motifs clearly for three-layer clusters ( $n > 55$ ), we were unsuccessful in doing so for smaller, two-layer clusters. This problem may be resolved in the future if an appropriate order parameter is found.

Our results indicate that the quantum delocalization, besides softening, also effectively increases the range of the particle-particle interaction, which happens to induce the same sequence of structural transitions.<sup>4,28,29</sup> Furthermore, the quantum  $n$ - $\Lambda$  ( $T = 0$ ) phase diagram revealed similarities with the classical  $n$ - $T$  ( $\Lambda = 0$ ) diagram,<sup>8,11</sup> which again supported the view that the quantum-induced transitions are akin to the thermally induced transitions. However, one should not go too far in trying to account for the quantum effects by introducing the “effective temperature” because the  $\Lambda \rightarrow T$  mapping is not universal, that is, not only is it size-specific but also the classical and quantum diagrams have certain qualitative differences.

We believe that our results are generally correct for the weakly quantum regime that at least includes the neon clusters, but they may only be qualitatively correct for the more quantum regime, perhaps starting with H<sub>2</sub> clusters. When the quantum effects are sufficiently strong, the Gaussian approximation may fail to describe the delocalized ground-state wave function adequately. Moreover, it is believed that the particle exchange symmetry becomes important, at least for hydrogen clusters and may even result in superfluidity,<sup>20,21</sup> whereas this effect is not accounted for within the present approximation. At the same time, because of the sampling problems, the PIMC and related methods may be hard to apply in the weakly quantum regime, whereas they become much better suited for the strongly quantum regime.

Molecular beams of rare-gas clusters are commonly prepared by a free jet expansion, as detailed in refs 30–34. The cluster size distribution, particularly, the mean size, can be controlled by tuning certain experimental parameters.<sup>30,31</sup> However, methods for the structural characterization of clusters are limited, as many techniques disrupt the fragile atomic arrangements, leading to a loss of structural information.<sup>32,35</sup> Electron diffraction methods have proven to be most successful in elucidating structural data of rare-gas clusters and therefore serve as the principle tool for examining cluster geometry.<sup>30–35</sup> In refs 30 and 31, electron diffraction was used to characterize the structure of Ar<sub>n</sub> clusters effectively, where for  $20 < n < 50$ , the configurations were based on the polyicosahedral motif, whereas for  $50 < n < 750$ , the multilayer icosahedron was the principle structure. The above authors also revealed the presence of two subtypes that differ in the overlayer packing, where a regular or (Mackay) ordering was encountered for  $n \approx 75$  to  $115$  (yielding an incomplete icosahedron); for sizes  $n < 75$ , a more disordered “twin” packing was observed.

It therefore seems feasible to extend the aforementioned experimental methods to different cluster types and size ranges to characterize their structure and substantiate our predictions further. Further evidence of our findings could be obtained by more systematic studies of Ar<sub>n</sub> and (more quantum) rare-gas, for example, Ne<sub>n</sub>, or molecular, (D<sub>2</sub>)<sub>n</sub> or (H<sub>2</sub>)<sub>n</sub>, clusters.

**Acknowledgment.** This work was supported by the NSF grant CHE-0809108. We acknowledge the contribution of Pavel Frantsuzov in writing a significant part of the code used for the present calculations. We also thank David Wales for many useful discussions. The data used to construct Figure 8 was provided by Cheng and Yang.

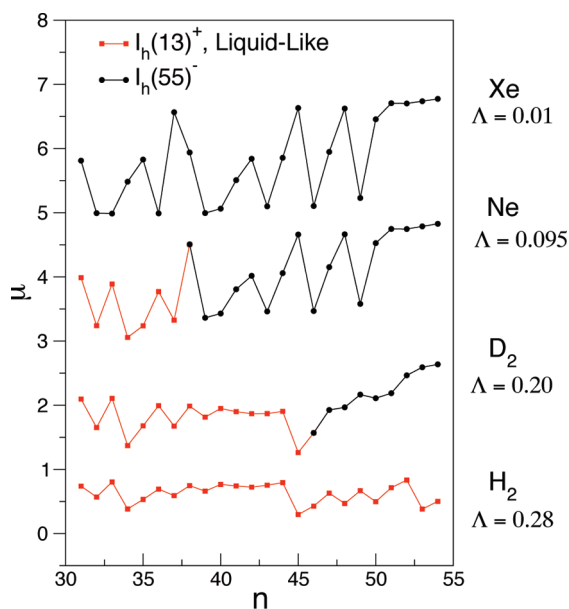


**Figure 10.** Chemical potential  $\mu(n)$  (in units of  $\epsilon$ ), as defined by eq 18, for the size range of 31–55 and for values of quantum parameter ( $\Lambda$ ) corresponding to those of Xe, Ne, D<sub>2</sub>, and H<sub>2</sub>. The quantum effects both reduce and soften the effective interaction between the particles, which explains the trends seen. In addition, strong correlations between the  $\mu(n)$  dependencies at different  $\Lambda$  values exist in regions that share the same ground-state motif (indicated by color).

## References and Notes

- (1) Northby, J. A. *J. Chem. Phys.* **1987**, *87*, 6166.
- (2) Leary, R. H. *J. Global Optimization* **1987**, *11*, 35.
- (3) Doye, J. P. K.; Calvo, F. *J. Chem. Phys.* **2002**, *116*, 8307.
- (4) Cheng, L.; Yang, J. *J. Phys. Chem.* **2007**, *111*, 5287.
- (5) (a) Geyer, C. J. In *Computing Science and Statistics*, Proceedings of the 23rd Symposium on the Interface; Keramigas, E. M., Ed.; Interface Foundation: Fairfax, VA, 1991; pp 156–163. (b) Hukushima, K.; Nemoto, K. *J. Phys. Soc. Jpn.* **1996**, *65*, 1604.
- (6) (a) Neirotti, J. P.; Calvo, F.; Freeman, D. L.; Doll, J. D. *J. Chem. Phys.* **2000**, *112*, 10340. (b) Calvo, F.; Neirotti, J. P.; Freeman, D. L.; Doll, J. D. *J. Chem. Phys.* **2000**, *112*, 10350.
- (7) Frantz, D. D. *J. Chem. Phys.* **2001**, *115*, 6136.
- (8) Mandelshtam, V. A.; Frantsuzov, P. *J. Chem. Phys.* **2006**, *124*, 204511.
- (9) Noya, E. G.; Doye, J. P. K. *J. Chem. Phys.* **2006**, *124*, 104503.
- (10) Mandelshtam, V. A.; Frantsuzov, P. A.; Calvo, F. *J. Phys. Chem. A* **2006**, *110*, 5326.
- (11) Sharapov, V. A.; Mandelshtam, V. A. *J. Phys. Chem. A* **2007**, *111*, 10284.
- (12) Chakravarty, C. *J. Chem. Phys.* **1995**, *103*, 10663.
- (13) Calvo, F.; Doye, J. P. K.; Wales, D. J. *J. Chem. Phys.* **2001**, *114*, 7312.
- (14) Predescu, C.; Frantsuzov, P. A.; Mandelshtam, V. A. *J. Chem. Phys.* **2005**, *122*, 154305.
- (15) Deckman, J.; Frantsuzov, P. A.; Mandelshtam, V. A. *Phys. Rev. E* **2008**, *77*, 052102.
- (16) (a) Predescu, C.; Sabo, D.; Doll, J. D.; Freeman, D. L. *J. Chem. Phys.* **2003**, *119*, 12119. (b) Sabo, D.; Predescu, C.; Doll, J. D.; Freeman, D. L. *J. Chem. Phys.* **2004**, *121*, 856.
- (17) Frantsuzov, P. A.; Meluzzi, D.; Mandelshtam, V. A. *Phys. Rev. Lett.* **2006**, *96*, 113401.
- (18) Predescu, C. Private communication.
- (19) Guardiola, R.; Navarro, J. *Cent. Eur. J. Phys.* **2008**, *6*, 33–37.
- (20) (a) Mezzacapo, F.; Boninsegni, M. *Phys. Rev. A* **2007**, *7*, 5–033201. (b) *Phys. Rev. Lett.* **2008**, *100*, 145301.
- (21) Khairallah, S. A.; Sevryuk, M. B.; Ceperley, D. M.; Toennies, J. P. *Phys. Rev. Lett.* **2007**, *9*, 8–183401.
- (22) Cuervo, J. E.; Roy, P.-N. *J. Chem. Phys.* **2008**, *128*, 224509.
- (23) Frantsuzov, P.; Mandelshtam, V. A. *J. Chem. Phys.* **2004**, *121*–9247.
- (24) Corbin, N.; Singer, K. *Mol. Phys.* **1982**, *46*, 671.
- (25) Frantsuzov, P.; Mandelshtam, V. A. *J. Chem. Phys.* **2008**, *128*, 094304.
- (26) Cambridge Cluster Database, [www.http://www-wales.ch.cam.ac.uk/CCD.html](http://www-wales.ch.cam.ac.uk/CCD.html).
- (27) Steinhardt, P. J.; Nelson, D. R.; Ronchetti, M. *Phys. Rev. B* **1983**, *28*, 784.
- (28) Doye, J. P. K.; Wales, D. J.; Berry, R. S. *J. Chem. Phys.* **1995**, *103*, 4234.
- (29) Doye, J. P. K.; Wales, D. J. *Science* **1996**, *271*, 484.
- (30) Farges, J.; de Feraudy, M. F.; Raoult, B.; Torchet, G. *J. Chem. Phys.* **1984**, *78*, 5067–5080.
- (31) Farges, J.; de Feraudy, M. F.; Raoult, B.; Torchet, G. *J. Chem. Phys.* **1986**, *84*, 3491–3501.
- (32) Borve, K. *J. Phys. Chem. Chem. Phys.* **2006**, *8*, 1891–1898.
- (33) van de Waal, B. W.; Torchet, G.; de Feraudy, M. F. *Chem. Phys. Lett.* **2000**, *331*, 57–63.
- (34) Danylchenko, O. G.; Kovalenko, S. I.; Samovarov, V. N. *Low. Temp. Phys.* **2004**, *30*, 166–170.
- (35) Amar, F. G.; Smaby, J.; Preston, T. J. *J. Chem. Phys.* **2005**, *122*, 244717.

JP900095F